ACS OMEGA

Open Access

http://pubs.acs.org/journal/acsodf

Article

Plasmon-Enhanced Refractive Index Sensing of Biomolecules Based on Metal−Dielectric−Metal Metasurface in the Infrared Regime

Ghulam Abbas Khan,* Yonghua Lu, and Pei Wang

Cite This: *ACS Omega* 2024, 9, 1416−1423

Read Online

ACCESS | Metrics & More | Article Recommendations

ABSTRACT: Infrared plasmonic sensors offer enhanced biomolecule detection potential over visible sensors due to unique spectral fingerprints, enhanced sensitivity, lower interference, and label-free, nondestructive analysis capabilities. Moreover, multimode plasmonic sensors are highly advantageous for their ability to outperform single-mode counterparts through long-wavelength tuning, enhanced information retrieval, and reduced false results through multimode data cross-referencing. In this study, to achieve a high quality factor and enhanced sensitivity simultaneously, we employed silver square block arrays (SSBs) in a metal−dielectric−metal configuration. The proposed design supports three modes resulting from gap plasmons and propagating surface plasmon resonances, enabling the detection of a broad spectrum of biomolecules. Designed sensors demonstrate notable sensitivities in different modes: Mode I achieves 525 nm/RIU, Mode II reaches 1287 nm/RIU, and Mode III records 812 nm/RIU, while maintaining the quality factor of Mode I—17, Mode II—356, and Mode III—107. The figure of merit for Mode I is 7 RIU^{-1}, for Mode II it is 375 RIU^{-1}, and for Mode III it is 98 RIU^{-1}. Different concentrations of glucose and hemoglobin are efficiently detected with the proposed sensor, showing great potential for its biosensing application and real-time monitoring of biomolecule dynamics. Taken together, the proposed sensor exhibits the capability to identify diverse types of biomolecules and holds the potential to serve as a preliminary screening tool for various biomolecules.

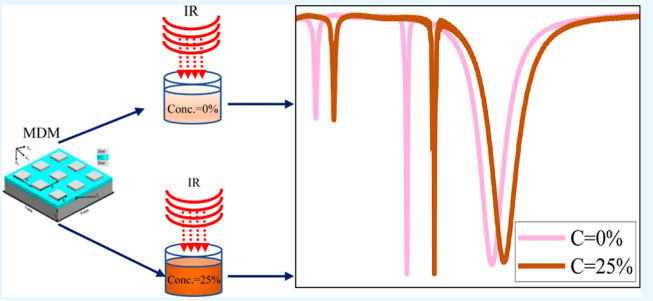

INTRODUCTION

Biosensors have the potential to facilitate early disease diagnosis and enable real-time patient monitoring through the detection of certain biomolecules. They can be operated effortlessly by individuals without specialized expertise.[1−7] It is worth mentioning that optical sensors provide a platform characterized by their high sensitivity and contact-free, exceptional resolution. This has spurred comprehensive research directed toward creating a multitude of applications, including point-of-care diagnostics, the detection of molecular fingerprints in the mid-infrared range, and the design of deployable sensors for various settings.[8−10] Infrared optical sensors efficiently detect and characterize bioanalytes by matching their wavelength to molecular vibrations, revealing specific structural information and enabling precise and sensitive detection of biomolecules in medical, environmental, and food safety applications.

In recent decades, optical biosensors employing refractive index (RI) sensing have emerged as a noteworthy category with a highly promising future.[11−15] Localized surface plasmon resonance (LSPR) mediated by gold nanorods patterned on graphene was also realized for biomolecule detection.[16] Although graphene has promising potential to bind with aromatic rings of biomolecules through $\pi-\pi$ stacking interaction, LSPR is primarily confined to gold nanorods, limiting its ability to adequately cover long-chain biomolecules.[17] Metals such as, gold, silver, and aluminum were utilized to realize plasmonic sensors capable of sustaining surface plasmon polariton resonant modes.[18−20] These modes exhibit remarkable benefits, encompassing rapid one-step detection, label-free, noninvasive characteristics, and effective coverage of biomolecules. Silver exhibits higher sensitivity to changes in background RI than gold and aluminum in the optical and infrared regimes.[21] Single-mode optical sensors detect biomolecules but have an inherent risk of errors due to limited information retrieval and the absence of redundant confirmation in a single resonance mode.[22,23] In contrast, multiple resonance modes provide improved information retrieval, redundant verification, and enhanced sensitivity. Consequently, these biosensors hold substantial potential for

Received: October 7, 2023
Revised: December 11, 2023
Accepted: December 13, 2023
Published: December 29, 2023

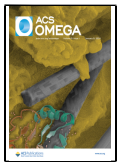

diverse applications such as measuring media concentration, identifying individual cancer cells, and performing nucleic acid−based analysis.[24−26]

Metal-based biosensors typically offer greater sensitivity owing to enhanced electric fields, but they often suffer from lower quality factors due to the presence of metal-induced ohmic losses.[15] Conversely, dielectric-based biosensors achieve high-quality sensing modes but have limited sensitivity to background RI changes because their optical modes are mainly confined within the dielectric material. To overcome this challenge, hybrid nanostructures can effectively enhance electric fields and enable higher energy confinement in ultrathin gap.[27,28] Additionally, propagating surface plasmon (PSP) and gap surface plasmon resonance (GSP) are employed for the realization of biosensors due to their higher sensitivity.[29,30] It makes them fit for tasks demanding higher sensitivity and an efficient response to variation in the RI of their surrounding environment.

It is essential for an efficient plasmonic sensor to exhibit a high-quality factor and a good figure of merit (FoM) simultaneously for efficient detection of biomolecules. This work proposes a hybrid metasurface in metal−dielectric−metal (MDM) configuration, comprising silver square block arrays (SSBs) placed on spacers and backed by a silver reflector. The finite difference time domain (FDTD) method is employed to investigate the designed plasmonic metasurface. This study reveals the emergence of three resonance modes resulting from the interaction of surface plasmon and gap plasmon. The emergent resonance modes demonstrated exceptional performance: Mode I exhibited 525 nm/RIU sensitivity with a quality factor of 17, Mode II achieved 1287 nm/RIU sensitivity with a quality factor of 356, and Mode III reached 812 nm/RIU sensitivity with a quality factor of 107. The FoM for Mode I is 7 RIU^{-1}, for Mode II it is 375 RIU^{-1}, and for Mode III it is 98 RIU^{-1}. Furthermore, various concentrations of glucose and hemoglobin are accurately detected by the proposed sensor, highlighting its strong potential for biosensing applications and real-time monitoring of biomolecule dynamics.

RESULTS AND DISCUSSION

The proposed metasurface comprised SSBs placed on a silver reflector and separated by a silica spacer. Silica spacer thickness is represented by "t_s" and RI (n_D = 1.45). The silver reflector thickness is chosen to be 100 nm. The geometrical parameters of SSBs are shown in Figure 1, lateral periodicity along the x and y axes is denoted by "P", side length "w", and thickness "h". The FDTD method is used to study the origin of supported optical modes on the metasurface. A plane wave source with an amplitude of E_0, linearly polarized along the x-axis (TM-wave),

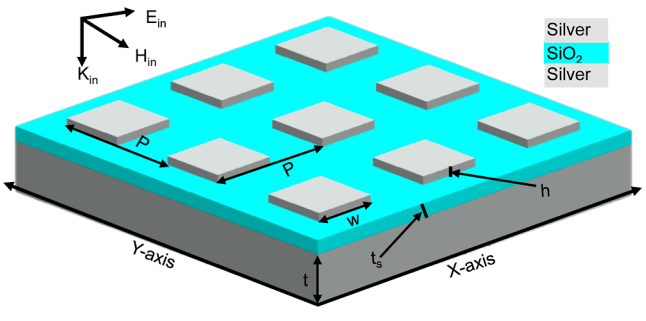

Figure 1. Schematic diagram of the proposed MDM metasurface.

is illuminated on the metasurface at normal incidence. In the lateral directions (x,y) periodic conditions are employed, and perfect boundary conditions are implemented in the ± z direction of the metasurface. The background RI is chosen to n = 1.33 in the entire simulation. The silver permittivity is obtained from the Lorentz−Drude model[31] as this model is essentially employed to calculate the frequency-dependent complex dielectric function $\epsilon_m(\omega)$.

Reflectance, absorbance, and transmittance spectra are illustrated in Figure 2; three dips (peaks) are prominent in

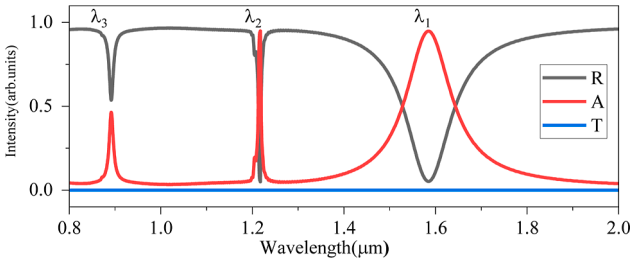

Figure 2. Reflectance, absorbance, and transmittance spectra of the metasurface at fixed background RI = 1.33, periodicity P = 900 nm, w = 270 nm.

reflectance (absorbance) spectra, whereas transmission is limited to zero. These spectra are calculated while the physical parameters of the metasurface were fixed at w = 270 nm, t_s = 30 nm, P = 900 nm, h = 50 nm, and background RI n = 1.33. The dips(peaks) in the reflectance (absorbance)spectra indicate the excitation of three distinct resonance modes referred to as mode I (λ_1 = 1584 nm), mode II (λ_2 = 1215 nm), and mode III (λ_3 = 890 nm) when the light interacts with the metasurface. The reflectance at resonance modes I and II is nearly zero, suggesting a strong coupling of incident light energy to these modes. The coupling strength of resonance mode III is weaker compared to modes I and II. In our metasurface, the SSBs placed on spacers and backed by a silver reflector facilitate guidance and confinement of mode I in spacers. The resonant wavelength of mode I is related to the size of SSBs and spacer thickness. The array of SSBs acts as two-dimensional gratings, inducing extra momentum $G = \frac{2\pi}{p}\sqrt{(l^2 + m^2)}$,[32] where p is the grating constant, l and m are integers. This additional momentum facilitates the excitation of the PSP on the surface of SSBs. Mode II and III observed in the reflectance spectrum are associated with (l, m) = (1,0) and (l,m) = (1,1), respectively. The resonance wavelength for both modes is directly related to the grating period P.

The physical principle behind the emergence of the three modes can also be elucidated by examining the enhanced electric field profile corresponding to these modes. The electric field profile associated with mode I (λ_1) in Figure 3a is calculated at the surface of SSBs, and in Figure 3b, it is calculated at the surface of the reflector in the XY plane. The same profile is depicted in Figure 3c in the XZ plane. The observed electric field profile exhibits that it is localized on the corners of SSBs and highly confined in the silica spacer, resulting in the emergence of two hotspots. The radiating electric dipole undergoes multiple reflections between the edges of SSBs and the silver reflector, resulting in high confinement within the spacer layer, as shown in Figure 3c.

https://doi.org/10.1021/acsomega.3c07809
ACS Omega 2024, 9, 1416−1423

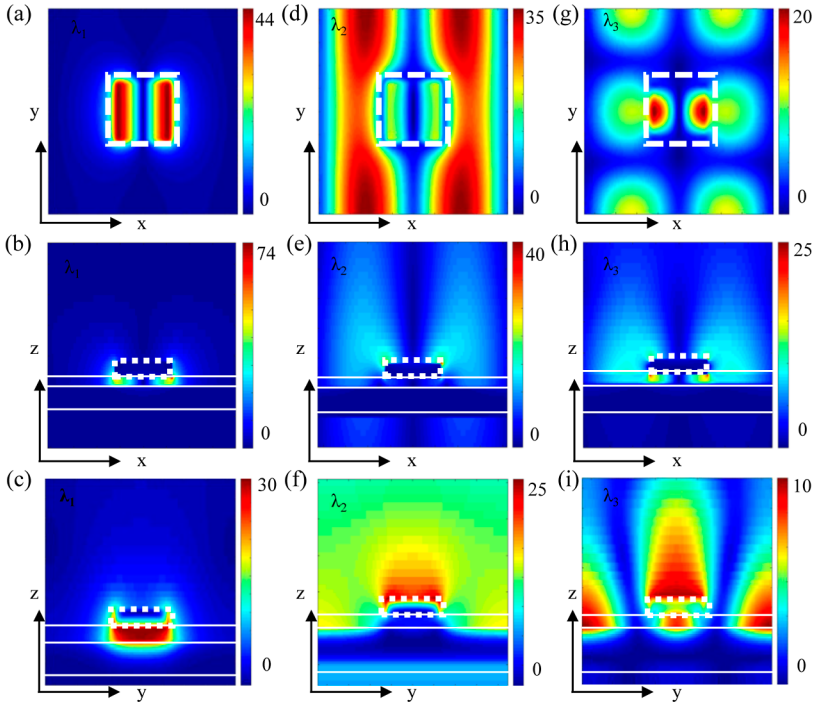

Figure 3. Electric field distribution: top row on the top surface of the silver reflector in the XY plane, middle row at the top surface of SSBs in the XY plane, and bottom row in the XZ plane of three resonant modes. (a−c) Resonant mode I(λ_1), (d−f) resonant mode II(λ_2), and (g−i) resonant mode I(λ_3). Rectangular dotted frames highlight the boundary of SSBs, and straight white lines depict the interface between silver and silica.

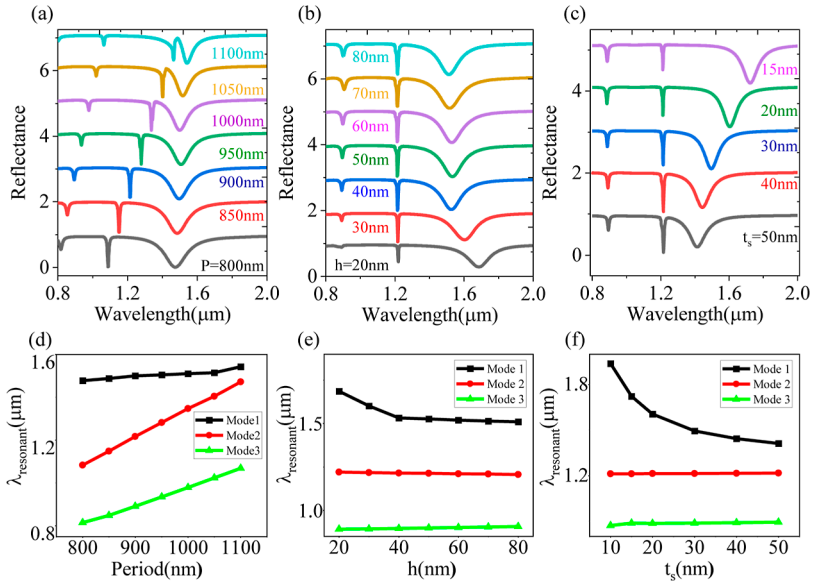

Figure 4. Dependence of geometrical parameters on resonant modes. (a−c) Influence of changing periodic distance P, SSB thickness h, and spacer thickness t_s, respectively. (d−f) Resonant wavelength shifts for mode I, mode II, and mode III corresponding to changes in (a−c).

Hence, this GSP radiates in dipole behavior and is confined in a very thin spacer layer.

Figure 3d,e shows the electric field distribution for mode II in the XY plane, while Figure 3f depicts the same profile in the XZ plane. It is evident from the electric field distribution signature that most of the field is delocalized in nature and spreading along the y-axis. Figure 3g−h illustrates the electric field distribution in XY, while Figure 3i shows the same profile in the XZ plane. The electric field distribution clearly indicates partial localization of the field at the surface of SSBs and within the spacer. However, a substantial portion of the field spreads out beyond the position of SSBs, as shown in Figure 3i. After careful examination of the electric field distribution associated with mode II and mode III, it is concluded that the incident light energy converts to PSP and exhibits radiating dipole behavior at different grating orders. Specifically, mode II is excited in the $(l,m) = (1,0)$ direction, while mode III is excited in the $(l,m) = (1,1)$ direction.

Figure 4 presents the analysis of reflectance spectra, revealing the relationship between emergent resonant modes and key geometrical parameters of the proposed hybrid metasurface. Figure 4a represents the reflectance spectra for

https://doi.org/10.1021/acsomega.3c07809
ACS Omega 2024, 9, 1416−1423

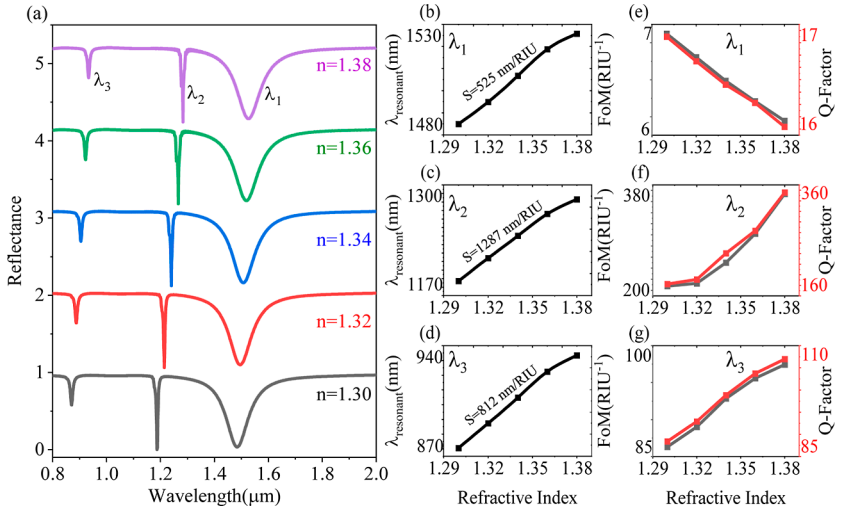

Figure 5. (a) Fine-tuning of resonant modes with respect to background RI at a fixed periodicity of P = 900 nm and w = 250 nm. (b–d) Resonant wavelength shift of modes I, II, and III, respectively. (e–g) FoM and Q-factor for modes I, II, and III, respectively.

varying periodic distances of SSBs, ranging from P = 800 nm to P = 1100 nm at 50 nm intervals. Notably, as the periodic distance increases, the resonant modes II and III switch their positions to longer wavelengths. This trend can be attributed to modifications in the respective wave vectors resulting from the changing distance among the SSBs, as depicted in Figure 4d. Conversely, mode I exhibits a slight change in resonance position, primarily impacted by an increased aspect ratio. It suggests that mode I was mainly confined in the spacer layer and did not switch its resonance behavior significantly due to an increase in the periodic distance.

Figure 4b depicts the reflectance spectra as the thickness of SSBs is varied from 20 to 80 nm in the interval of 10 nm. The resonant modes II and III maintain their positions, while mode I demonstrates a blueshift as the 'h' increases from 20 to 80 nm. Initially, it exhibits a decreasing trend in shift, but later, it follows a parallel trend to the x-axis, as shown in Figure 4e. As the spacer thickness t_s is changed from 15 to 50 nm, mode I exhibits a blue shift, which can be well explained by capacitance induced by SSBs and silver reflectors.[27] Such capacitance can be mathematically expressed as $C \sim S/t_s$[27], where C is the capacitance, S is the area of the SSBs and silver reflector, and t_s is the thickness of the spacer layer. Notably, capacitance is in inverse relationship to spacer thickness; as the thickness increases, the capacitance tends to decrease, which influences the entire system to shift toward higher energy. The fine-tuning of mode I and mode II is achieved by changing the periodic distance, while mode I is finely tuned by changing spacer thickness t_s and SSBs thickness h. The proposed metasurface exhibits promising potential for the efficient fine-tuning of three resonance modes by carefully selecting different geometrical parameters. The capability of resonance mode shifting enables long-range biomolecule sensing by modifying the background RI of these proposed sensors.

Figure 5a illustrates the tunability of modes with respect to changes in background RI. As the RI changed from n = 1.30 to n = 1.38 in the step of 0.02, three modes exhibited a shift in resonant wavelength toward a longer wavelength. Starting at an initial RI of 1.3, the resonance mode I emerges at 1484 nm. As the RI gradually increases to 1.38, mode I undergoes a noticeable shift to 1526 nm, as shown in Figure 5b. The sensor sensitivity is characterized as $S = \frac{\Delta\lambda}{\Delta n}$, where $\Delta\lambda$ is the shift in resonant wavelength corresponding to a change in RI Δn.[33] The sensitivity for mode I is computed to be approximately 525 nm/RIU. The FoM is the measure of sensing performance of the optical biosensor, which is defined as FoM = $\frac{S}{\text{FWHM}}$, where S is the sensitivity of the RI sensor and fwhm is the fullwidth of half-maximum.[33] FoM for mode I is achieved at about 7 RIU^{-1}, as depicted in Figure 5e. The quality factor, denoted as Q, provides insights into the radiation and energy confinement of an optical cavity, expressed as $Q = \frac{\lambda_{\text{resonant}}}{\text{FWHM}}$.[33] The higher quality factors are indicative of higher sensor efficiency, and resonant mode I achieves a quality of 17, as shown in Figure 5e. Figure 5c depicts the resonant shift within mode II, ranging from 1187 to 1290 nm due to variation in the RI from n = 1.3 to n = 1.38. Mode II exhibits a sensitivity of approximately 1287 nm/RIU, accompanied by a quality factor spanning from 160 to 360, and its FOM varies within the range of 200–380, as shown in Figure 5f. Figure 5d shows the shift in resonant mode III, spanning from 870 to 935 nm, as the RI varies within the range of n = 1.3 to n = 1.38. Mode III demonstrates a sensitivity of around 812 nm/RIU, with a quality factor ranging from 96 to 117, and its FOM varies within the range of 90–101, as shown in Figure 5g. Since three modes are efficiently tuned and maintain a good FoM and q factor simultaneously as the background RI is changed, these modes have the potential to retrieve detailed information about the sensing analytes across a broad spectrum.

Biosensing Applications. Optical sensors used in biosensing frequently encounter challenges arising from the absorption fingerprint of biomolecules, which can interfere with the resonance modes and lead to inaccurate results. To address this issue, we have employed three sensing modes spanning a wavelength range of 800–1600 nm. This approach enhances data retrieval and allows for cross-referencing confirmation through the utilization of three distinct resonance modes. Three distinct resonance modes emerged due to GSP and PSP being employed to realize the biosensing applications for the detection of glucose and hemoglobin molecules in the subsequent analysis.

Diabetes Diagnosis. The concentration of blood glucose depicts the quantity of glucose present in a specific volume of blood, serving as a vital source of energy for the body. It is

https://doi.org/10.1021/acsomega.3c07809
ACS Omega 2024, 9, 1416–1423

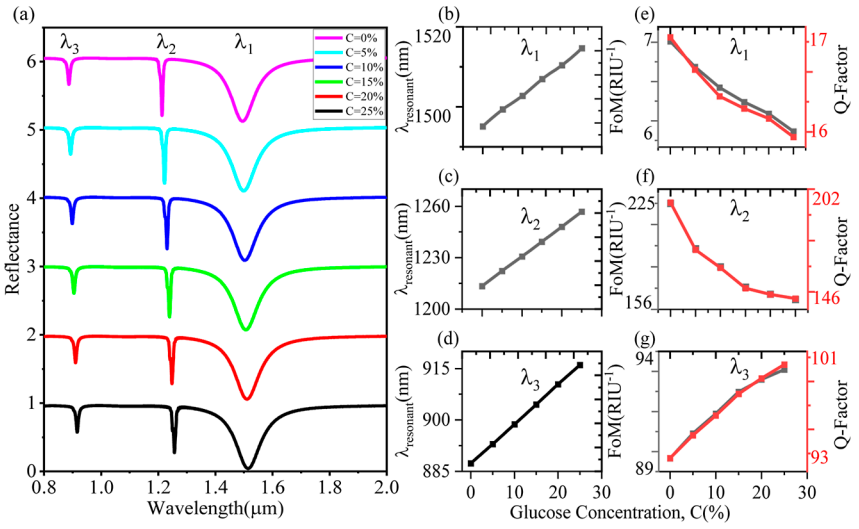

Figure 6. (a) Reflectance spectra for different concentrations of glucose in blood. (b–d) Shift in resonant modes as glucose concentration in blood has varied. (e–g) FoM and *Q*-factor for modes I, II, and III, respectively.

essential to regulate glucose levels to ensure a consistent energy supply for the body. Generally, glucose levels in blood vary throughout the day and are also influenced by numerous factors such as age, meal timing, and overall health. The RI related to distinct glucose concentrations in blood can be determined by the following equation.[34]

$$n = 0.2015 \times C\ \% + 1.3292$$

where n represents RI and C % denotes the glucose concentration. Our simulations accurately replicate the scenario where a metasurface is immersed in different concentrations of glucose, ranging from C = 0% to C = 25%. Consequently, the emerging resonance modes undergo shifts in their positions, as shown in Figure 6a–d. The shift in mode I from 1495 to 1515 nm as glucose concentration varies from C = 0% to C = 25%, as shown in Figure 6b. Mode I achieves a sensitivity of 525 nm/RIU, a FoM of 7 RIU^{-1}, and a Q factor of 17, as represented in Figure 6e. The modulation in mode II is observed from 1213 to 1257 nm as the glucose concentration undergoes a change from C = 0% to C = 25%, as illustrated in Figure 6c. Mode II exhibits sensitivity of 1287 nm/RIU, dynamic FoM spanning from 156 RIU^{-1} to 225 RIU^{-1}, and a Q factor ranging from 146 to 202, as shown in Figure 6f. The transition of mode III is demonstrated in Figure 6d, moving in the range of 887–916 nm and maintaining sensitivity of 812 nm/RIU. Accompanying this shift, FoM varies from 89 to 94 RIU^{-1}, and the Q factor spans from 93 to 101. Since three resonance modes modulate their spatial position efficiently and maintain good FoM and a high Q factor simultaneously, this metasurface functions well for the detection of distinct concentrations of glucose.

Each mode is calibrated according to a distinct concentration of glucose; this metasurface enables the validation of results by comparing data collected from the three modes, eventually enhancing sensitivity and reliability. Furthermore, biological fluids such as blood comprise different substances that can mislead the single-mode biosensor, eventually generating false readings. Hence, our proposed sensor based on three peaks mitigates the risk of false readings influenced by an interfering compound because all peaks would be unaffected simultaneously. This redundancy is critical in managing conditions such as diabetes, where patients depend on precise and reliable glucose monitoring to manage their health. A false reading can lead to inappropriate insulin administration, which can have serious, even life-threatening, consequences. Multi-peak sensors mitigate this risk, offering peace of mind and a higher level of safety for users.

Furthermore, the unknown glucose concentration can be easily determined by utilizing the aforementioned relationship. This percentage concentration typically can be converted to molar concentration in millimoles per liter (mmol/L), which enables easy and rapid assessment of the severity of diabetes. Prior to proceeding with the calculation of molar concentration, it is important to know the molecular weight and density of the solution. At standard conditions (room temperature and atmospheric pressure), the density of pure glucose (also to referred as anhydrous dextrose) is approximately 1.54 g/mL, and the molecular weight is approximately 180.16 g/mol. The following expression can be used to find the diabetic level (mmol/L).[35]

$$\text{diabetes level} = \frac{\text{concentration (\%)} \times \text{density in g/mL} \times 1000}{\text{molecular weight}}$$

Table 1 is calculated based on the above equation to assess whether the glucose sample falls within the healthy, prediabetic, or diabetic range. It provides a means of categorizing the glucose levels and determining the corresponding condition.

Table 1. Classification of Diabetes

condition	RI	range (mmol/L)	concentration (%)
diabetic	>1.3317	>11	>1.286
prediabetic	1.3310–1.3317	7.8–11	0.912–1.286
healthy	<1.3310	<7.8	0.912

Anemia Type Detection. Hemoglobin is an essential protein in red blood cells which plays a crucial role in carrying oxygen from the lungs to the body's tissues and also transporting carbon dioxide from tissues to the lungs for elimination during exhalation. The measure of hemoglobin concentration manifests the level of hemoglobin in blood. A

https://doi.org/10.1021/acsomega.3c07809
ACS Omega 2024, 9, 1416–1423

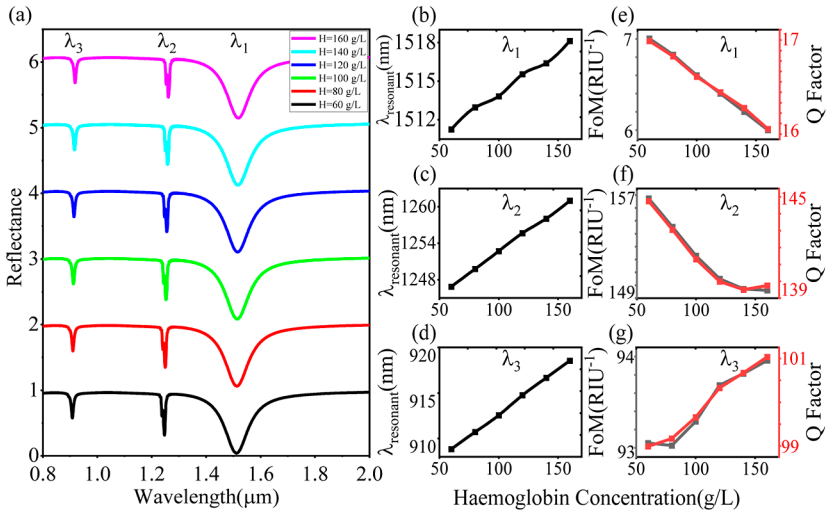

Figure 7. (a) Reflectance spectra for different concentrations of hemoglobin. (b–d) Three resonant modes shifting as hemoglobin in blood has varied. (e–g) FoM and *Q*-factor for modes I, II, and III, respectively.

deficiency in the level of hemoglobin in blood is indicative of anemia, a condition that arises when the body has an insufficient number of red blood cells or a low hemoglobin level to effectively transport oxygen to all body tissues.[36] The RI and hemoglobin concentrations can be linked by the following equations.[37]

$$n = 1.38 + \frac{1}{5766.5}(H - H_{\text{normal}})$$

where H_{normal} refers to the standard hemoglobin density for the human body, which is typically defined as 140 g/L, with a corresponding RI of 1.38.

The simulated reflectance spectra are demonstrated in Figure 7a as the metasurface is immersed in the different concentrations of hemoglobin samples. As the hemoglobin concentration varies from H = 60 g/L to H = 160 g/L, the resonance mode shifts its position, as depicted in Figure 7b–d. Mode I exhibits a wavelength shift from 1511 to 1518 nm, Mode II shows a transition from 1246 to 1261 nm, and mode III demonstrates a shift of 908–918 nm. The FoM and *Q* factor for these modes are as follows: mode I has an FoM of 6 RIU^{-1} and a *Q* factor of 16, mode II has an FoM of 156 RIU^{-1} and a *Q* factor of 144, and mode III has an FoM of 93 RIU^{-1} and a *Q* factor of 101. Since the random concentration of hemoglobin in blood can be efficiently detected through the observed shift in resonance modes. A multimode approach ensures accurate readings and addresses the susceptibility of single-mode sensors to confounding factors in blood samples. Multimode sensors provide independent assessments of hemoglobin content, offering a crucial cross-checking mechanism. This functionality is vital for conditions where precise hemoglobin levels are critical, such as anemia or blood disorders. Furthermore, anemia can easily be diagnosed by observing the decrease in hemoglobin value compared to that of standard H_{normal}. The severity of anemia can be categorized further depending on the observed value in the blood sample, as described in Table 2. On the other hand, an increase in hemoglobin concentration above H_{normal} can indicate the presence of polycythemia, a condition in which the body generates an excessive number of red blood cells that can cause blood clotting in the human body.[38]

Table 2. Primary Categories of Anemia

condition	RI	range (g/L)
acute	<1.369	<80
moderate	1.369–1.373	80–100
minor	1.373–1.376	100–120
healthy	>1.376	>120

The biological applications of our proposed sensor were discussed and realized in the preceding discussion. In this section, we describe a detailed comparison of our proposed plasmonic sensor with those of its previously reported counterparts. This comprehensive comparative analysis is presented in Table 3, offering valuable insights into the distinct advantages and advancements our sensor brings to the field of biosensing. It is evident that sensors utilizing metallic components experience a reduction in FoM and quality factors due to the presence of ohmic losses. Conversely, dielectric-

Table 3. Comparison Analysis of This Plasmonic Sensor With Other Sensors

refs	materials	structure	*S* (nm/RIU)	FoM (RIU^{-1})	*Q*
33	Au	elliptical metasurface	655	20	47
39	Ag	2D Ag nanowell crystals	623.7	55.2	67
40	Pt	2d-metallic photonic crystal slabs	571	2	5
41	Au	hybrid sensor based on LSPR	321	3.2	8
42	Au	asymmetric double split-ring resonators	520	2.9	6.2
9	Si	elliptical dielectric nano resonators	263	44	144
43	Si	all-dielectric rectangular bar and ring metasurface	289	103	483
44	Ag	cross shaped MIM cavity	1100	9.95×10^4	
this work	Ag–SiO_2	SSBs in MDM configuration	1287	375	356

https://doi.org/10.1021/acsomega.3c07809
ACS Omega 2024, 9, 1416–1423

based sensors exhibit limited sensitivity owing to the localized nature of the electric field within the dielectric material. Nevertheless, they consistently maintain high FoM and quality factors when compared with their metallic counterparts. In contrast, our proposed hybrid metasurface-based sensor stands out prominently in terms of sensitivity, FoM, and quality factors.

CONCLUSIONS

In summary, our research highlights the superiority of infrared plasmonic sensors for biomolecule detection, offering unique advantages over visible sensors. These include distinctive spectral fingerprints, enhanced sensitivity, reduced interference, and label-free, nondestructive analysis capabilities, making them promising for diverse applications. We introduced multimode plasmonic sensors using SSBs in the MDM configuration. This enabled the detection of a wide range of biomolecules by exploiting three distinct sensing modes arising from gap plasmons and PSP resonances. These modes demonstrated exceptional performance: Mode I exhibited 525 nm/RIU sensitivity with a quality factor of 17, Mode II achieved 1287 nm/RIU sensitivity with a quality factor of 356, and Mode III reached 812 nm/RIU sensitivity with a quality factor of 107. The FoM for Mode I is 7 RIU^{-1}, for Mode II it is 375 RIU^{-1}, and for Mode III it is 98 RIU^{-1}. Furthermore, this designed sensor efficiently detects various concentrations of glucose and hemoglobin, facilitating the assessment of diabetic and anemia conditions. Taken together, the proposed sensor exhibits the capability to identify diverse types of biomolecules and holds the potential to serve as a preliminary screening tool for various biomolecules.

ASSOCIATED CONTENT

Data Availability Statement

The data supporting the results presented in this paper has been comprehensively incorporated within the body of the paper itself.

AUTHOR INFORMATION

Corresponding Author

Ghulam Abbas Khan − *Department of Optics and Optical Engineering, University of Science and Technology of China, Hefei 230026, China;* orcid.org/0009-0001-8394-8977; Email: gakhan@mail.ustc.edu.cn

Authors

Yonghua Lu − *Department of Optics and Optical Engineering, University of Science and Technology of China, Hefei 230026, China;* orcid.org/0000-0003-1049-8474

Pei Wang − *Department of Optics and Optical Engineering, University of Science and Technology of China, Hefei 230026, China*

Complete contact information is available at: https://pubs.acs.org/10.1021/acsomega.3c07809

Notes

The authors declare no competing financial interest.

ACKNOWLEDGMENTS

This work was supported by the Natural Science Foundation of China (U20A20216) and the CAS-TWAS President's Fellowship for International PhD Students.

REFERENCES

(1) Liu, Y.; Wei, Z.; Zhou, J.; Ma, Z. Simultaneous Multi-Signal Quantification for Highly Precise Serodiagnosis Utilizing a Rationally Constructed Platform. *Nat. Commun.* **2019**, *10* (1), 5361.

(2) Schutgens, F.; Rookmaaker, M. B.; Margaritis, T.; Rios, A.; Ammerlaan, C.; Jansen, J.; Gijzen, L.; Vormann, M.; Vonk, A.; Viveen, M.; Yengej, F. Y.; Derakhshan, S.; de Winter-de Groot, K. M.; Artegiani, B.; van Boxtel, R.; Cuppen, E.; Hendrickx, A. P. A.; van den Heuvel-Eibrink, M. M.; Heitzer, E.; Lanz, H.; Beekman, J.; Murk, J.-L.; Masereeuw, R.; Holstege, F.; Drost, J.; Verhaar, M. C.; Clevers, H. Tubuloids Derived from Human Adult Kidney and Urine for Personalized Disease Modeling. *Nat. Biotechnol.* **2019**, *37* (3), 303−313.

(3) Masson, J.-F. Surface Plasmon Resonance Clinical Biosensors for Medical Diagnostics. *ACS Sens.* **2017**, *2* (1), 16−30.

(4) Cesewski, E.; Johnson, B. N. Electrochemical Biosensors for Pathogen Detection. *Biosens. Bioelectron.* **2020**, *159*, 112214.

(5) Li, J.; Liu, Y.; Yuan, L.; Zhang, B.; Bishop, E. S.; Wang, K.; Tang, J.; Zheng, Y.-Q.; Xu, W.; Niu, S.; Beker, L.; Li, T. L.; Chen, G.; Diyaolu, M.; Thomas, A.-L.; Mottini, V.; Tok, J. B.-H.; Dunn, J. C. Y.; Cui, B.; Paşca, S. P.; Cui, Y.; Habtezion, A.; Chen, X.; Bao, Z. A Tissue-like Neurotransmitter Sensor for the Brain and Gut. *Nature* **2022**, *606* (7912), 94−101.

(6) Jiang, Y.; Trotsyuk, A. A.; Niu, S.; Henn, D.; Chen, K.; Shih, C.-C.; Larson, M. R.; Mermin-Bunnell, A. M.; Mittal, S.; Lai, J.-C.; Saberi, A.; Beard, E.; Jing, S.; Zhong, D.; Steele, S. R.; Sun, K.; Jain, T.; Zhao, E.; Neimeth, C. R.; Viana, W. G.; Tang, J.; Sivaraj, D.; Padmanabhan, J.; Rodrigues, M.; Perrault, D. P.; Chattopadhyay, A.; Maan, Z. N.; Leeolou, M. C.; Bonham, C. A.; Kwon, S. H.; Kussie, H. C.; Fischer, K. S.; Gurusankar, G.; Liang, K.; Zhang, K.; Nag, R.; Snyder, M. P.; Januszyk, M.; Gurtner, G. C.; Bao, Z. Wireless, Closed-Loop, Smart Bandage with Integrated Sensors and Stimulators for Advanced Wound Care and Accelerated Healing. *Nat. Biotechnol.* **2023**, *41* (5), 652−662.

(7) Wei, Z.; Zhou, Z.-K.; Li, Q.; Xue, J.; Di Falco, A.; Yang, Z.; Zhou, J.; Wang, X. Flexible Nanowire Cluster as a Wearable Colorimetric Humidity Sensor. *Small* **2017**, *13* (27), 1700109.

(8) Tittl, A.; Leitis, A.; Liu, M.; Yesilkoy, F.; Choi, D.-Y.; Neshev, D. N.; Kivshar, Y. S.; Altug, H. Imaging-Based Molecular Barcoding with Pixelated Dielectric Metasurfaces. *Science* **2018**, *360* (6393), 1105−1109.

(9) Yesilkoy, F.; Arvelo, E. R.; Jahani, Y.; Liu, M.; Tittl, A.; Cevher, V.; Kivshar, Y.; Altug, H. Ultrasensitive Hyperspectral Imaging and Biodetection Enabled by Dielectric Metasurfaces. *Nat. Photonics* **2019**, *13* (6), 390−396.

(10) Zhang, L.; Fu, Q.; Tan, Y.; Li, X.; Deng, Y.; Zhou, Z.-K.; Zhou, B.; Xia, H.; Chen, H.; Qiu, C.-W.; Zhou, J. Metaoptronic Multiplexed Interface for Probing Bioentity Behaviors. *Nano Lett.* **2021**, *21* (6), 2681−2689.

(11) Martinsson, E.; Otte, M. A.; Shahjamali, M. M.; Sepulveda, B.; Aili, D. Substrate Effect on the Refractive Index Sensitivity of Silver Nanoparticles. *J. Phys. Chem. C* **2014**, *118* (42), 24680−24687.

(12) Shen, Y.; Zhou, J.; Liu, T.; Tao, Y.; Jiang, R.; Liu, M.; Xiao, G.; Zhu, J.; Zhou, Z.-K.; Wang, X.; Jin, C.; Wang, J. Plasmonic Gold Mushroom Arrays with Refractive Index Sensing Figures of Merit Approaching the Theoretical Limit. *Nat. Commun.* **2013**, *4* (1), 2381.

(13) Qin, J.; Jiang, S.; Wang, Z.; Cheng, X.; Li, B.; Shi, Y.; Tsai, D. P.; Liu, A. Q.; Huang, W.; Zhu, W. Metasurface Micro/Nano-Optical Sensors: Principles and Applications. *ACS Nano* **2022**, *16* (8), 11598−11618.

(14) Chen, Y.; Liu, J.; Yang, Z.; Wilkinson, J. S.; Zhou, X. Optical Biosensors Based on Refractometric Sensing Schemes: A Review. *Biosens. Bioelectron.* **2019**, *144*, 111693.

(15) Xu, Y.; Bai, P.; Zhou, X.; Akimov, Y.; Png, C. E.; Ang, L.; Knoll, W.; Wu, L. Optical Refractive Index Sensors with Plasmonic and Photonic Structures: Promising and Inconvenient Truth. *Adv. Opt. Mater.* **2019**, *7* (9), 1801433.

(16) Gao, X.; Li, L.; Deng, R.; Zhao, W.; Zhang, X.; Liu, Z. Localized Surface Plasmon Resonance-Modulated Graphene-Based Optical

Sensor for Ultrasensitive Immunoassays. *ACS Appl. Electron. Mater.* **2023**, *5* (2), 1140−1147.
(17) Song, B.; Li, D.; Qi, W.; Elstner, M.; Fan, C.; Fang, H. Graphene on Au(111): A Highly Conductive Material with Excellent Adsorption Properties for High-Resolution Bio/Nanodetection and Identification. *ChemPhysChem* **2010**, *11* (3), 585−589.
(18) Xomalis, A.; Tsilipakos, O.; Manousidaki, M.; Pérez De Gregorio Busquets, O.; Kenanakis, G.; Tzortzakis, S.; Farsari, M.; Soukoulis, C. M.; Economou, E. N.; Kafesaki, M. Enhanced Refractive Index Sensing with Direction-Selective Three-Dimensional Infrared Metamaterials. *ACS Appl. Opt. Mater.* **2023**, *1* (1), 10−16.
(19) Facchin, M.; Bruce, G. D.; Dholakia, K. Measurement of Variations in Gas Refractive Index with 10^{-9} Resolution Using Laser Speckle. *ACS Photonics* **2022**, *9* (3), 830−836.
(20) Chen, H.; Wang, X.; Zhang, J.; Rao, X.; Yang, H.; Qi, Y.; Tang, C. Theoretical Study of Surface Plasmonic Refractive Index Sensing Based on Gold Nano-Cross Array and Gold Nanofilm. *Phys. B* **2023**, *655*, 414746.
(21) Albrecht, G.; Ubl, M.; Kaiser, S.; Giessen, H.; Hentschel, M. Comprehensive Study of Plasmonic Materials in the Visible and Near-Infrared: Linear, Refractory, and Nonlinear Optical Properties. *ACS Photonics* **2018**, *5* (3), 1058−1067.
(22) Dell'Olio, F.; Su, J.; Huser, T.; Sottile, V.; Cortés-Hernández, L. E.; Alix-Panabières, C. Photonic Technologies for Liquid Biopsies: Recent Advances and Open Research Challenges. *Laser Photon. Rev.* **2021**, *15* (1), 2000255.
(23) Danaie, M.; Hajshahvaladi, L.; Ghaderpanah, E. A Single-Mode Tunable Plasmonic Sensor Based on an 8-Shaped Resonator for Cancer Cell Detection. *Sci. Rep.* **2023**, *13* (1), 13976.
(24) Xue, T.; Liang, W.; Li, Y.; Sun, Y.; Xiang, Y.; Zhang, Y.; Dai, Z.; Duo, Y.; Wu, L.; Qi, K.; Shivananju, B. N.; Zhang, L.; Cui, X.; Zhang, H.; Bao, Q. Ultrasensitive Detection of MiRNA with an Antimonene-Based Surface Plasmon Resonance Sensor. *Nat. Commun.* **2019**, *10* (1), 28.
(25) Xing, F.; Meng, G.-X.; Zhang, Q.; Pan, L.-T.; Wang, P.; Liu, Z.-B.; Jiang, W.-S.; Chen, Y.; Tian, J.-G. Ultrasensitive Flow Sensing of a Single Cell Using Graphene-Based Optical Sensors. *Nano Lett.* **2014**, *14* (6), 3563−3569.
(26) Mishra, A. K.; Mishra, S. K.; Verma, R. K. Graphene and Beyond Graphene MoS_2: A New Window in Surface-Plasmon-Resonance-Based Fiber Optic Sensing. *J. Phys. Chem. C* **2016**, *120* (5), 2893−2900.
(27) Khan, G. A.; Lu, Y.; Wang, P. Enhanced Dual-Band Absorption of Graphene Mediated by an Aluminum Metastructure. *2d Mater.* **2023**, *10* (3), 035032.
(28) Ji, D.; Cheney, A.; Zhang, N.; Song, H.; Gao, J.; Zeng, X.; Hu, H.; Jiang, S.; Yu, Z.; Gan, Q. Efficient Mid-Infrared Light Confinement within Sub-5-nm Gaps for Extreme Field Enhancement. *Adv. Opt. Mater.* **2017**, *5* (17), 1700223.
(29) Karki, B.; Salah, N. H.; Srivastava, G.; Muduli, A.; Yadav, R. B. A Simulation Study for Dengue Virus Detection Using Surface Plasmon Resonance Sensor Heterostructure of Silver, Barium Titanate, and Cerium Oxide. *Plasmonics* **2023**, *18*, 2031−2040.
(30) Mao, Z.; Peng, X.; Zhou, Y.; Liu, Y.; Koh, K.; Chen, H. Review of Interface Modification Based on 2D Nanomaterials for Surface Plasmon Resonance Biosensors. *ACS Photonics* **2022**, *9* (12), 3807−3823.
(31) Rakić, A. D.; Djurišić, A. B.; Elazar, J. M.; Majewski, M. L. Optical Properties of Metallic Films for Vertical-Cavity Optoelectronic Devices. *Appl. Opt.* **1998**, *37* (22), 5271.
(32) Chu, Y.; Crozier, K. B. Experimental Study of the Interaction between Localized and Propagating Surface Plasmons. *Opt. Lett.* **2009**, *34* (3), 244.
(33) Li, S.; Jiang, H.; Zhu, X.; Shi, Y.; Han, Z. A High-Sensitivity Refractive Index Sensor with Period-Doubling Plasmonic Metasurfaces to Engineer the Radiation Losses. *ACS Appl. Opt. Mater.* **2023**, *1* (3), 736−744.
(34) Liang, X.; Zhang, Q.; Jiang, H. Quantitative Reconstruction of Refractive Index Distribution and Imaging of Glucose Concentration by Using Diffusing Light. *Appl. Opt.* **2006**, *45* (32), 8360.
(35) Nugroho, H.; Hasanah, L.; Wulandari, C.; Pawinanto, R.; Haron, M. H.; Zain, A. R.; Berhanuddin, D.; Mulyanti, B.; Singh, P.; Menon, P. S. Silicon on Insulator-Based Microring Resonator and Au Nanofilm Krestchmann-Based Surface Plasmon Resonance Glucose Sensors for Lab-on-a-Chip Applications. *Int. J. Nanotechnol.* **2020**, *17* (1), 29.
(36) Xu, M.; Papageorgiou, D. P.; Abidi, S. Z.; Dao, M.; Zhao, H.; Karniadakis, G. E. A Deep Convolutional Neural Network for Classification of Red Blood Cells in Sickle Cell Anemia. *PLoS Comput. Biol.* **2017**, *13* (10), No. e1005746.
(37) Mostufa, S.; Paul, A. K.; Chakrabarti, K. Detection of Hemoglobin in Blood and Urine Glucose Level Samples Using a Graphene-Coated SPR Based Biosensor. *OSA Continuum* **2021**, *4* (8), 2164.
(38) Erslev, A. J.; Caro, J.; Kansu, E.; Miller, O.; Cobbs, E. Plasma Erythropoietin in Polycythemia. *Am. Med. J.* **1979**, *66* (2), 243−247.
(39) Ye, S.; Zhang, X.; Chang, L.; Wang, T.; Li, Z.; Zhang, J.; Yang, B. High-Performance Plasmonic Sensors Based on Two-Dimensional Ag Nanowell Crystals. *Adv. Opt. Mater.* **2014**, *2* (8), 779−787.
(40) Sarkar, S.; Ghosh, A. K.; Adnan, M.; Aftenieva, O.; Gupta, V.; Fery, A.; Joseph, J.; König, T. A. F. Enhanced Figure of Merit via Hybridized Guided-Mode Resonances in 2D-Metallic Photonic Crystal Slabs. *Adv. Opt. Mater.* **2022**, *10* (21), 2200954.
(41) Hao, D.; Hu, C.; Grant, J.; Glidle, A.; Cumming, D. R. S. Hybrid Localized Surface Plasmon Resonance and Quartz Crystal Microbalance Sensor for Label Free Biosensing. *Biosens. Bioelectron.* **2018**, *100*, 23−27.
(42) Zhao, J.; Zhang, C.; Braun, P. V.; Giessen, H. Large-Area Low-Cost Plasmonic Nanostructures in the NIR for Fano Resonant Sensing. *Adv. Mater.* **2012**, *24* (35), OP247.
(43) Yang, Y.; Kravchenko, I. I.; Briggs, D. P.; Valentine, J. All-Dielectric Metasurface Analogue of Electromagnetically Induced Transparency. *Nat. Commun.* **2014**, *5* (1), 5753.
(44) Yang, Q.; Liu, X.; Guo, F.; Bai, H.; Zhang, B.; Li, X.; Tan, Y.; Zhang, Z. Multiple Fano Resonance in MIM Waveguide System with Cross-Shaped Cavity. *Optik* **2020**, *220*, 165163.

https://doi.org/10.1021/acsomega.3c07809
ACS Omega 2024, 9, 1416−1423